Construction of MnO$_2$/Monolayer g-C$_3$N$_4$ with Mn vacancies for Z-scheme overall water splitting

Zhao Mo[a], Hui Xu[a,*], Zhigang Chen[a], Xiaojie She[a], Yanhua Song[b], Jiabiao Lian[a], Xingwang Zhu[a], Pengcheng Yan[a], Yucheng Lei[a], Shouqi Yuan[a], Huaming Li[a,*]

[a] School of Materials Science & Engineering, Institute for Energy Research, Jiangsu University, Zhenjiang 212013, PR China
[b] School of Environmental and Chemical Engineering, Jiangsu University of Science and Technology, Zhenjiang 212003, PR China

ARTICLE INFO

ABSTRACT

Defect-Engineering is a promising way to introduce metal cation vacancies into target materials, thereby resulting in excellent performance for photocatalytic or electrocatalytic water splitting. Inspired by this, we propose an efficient Z-scheme system comprised of 2D MnO$_2$/Monolayer g-C$_3$N$_4$ with defective Mn^{3+} active sites to realize overall water splitting. These defective Mn^{3+} active sites might boost H$_2$O adsorption and optimize the interfacial charge separation/transfer in the photocatalytic process by introducing the Mn^{3+}/Mn^{4+} redox couple. As a result, the composite displays an excellent and stable H$_2$ and O$_2$ evolution rates of 60.6 and 28.9 μmol g^{-1} h^{-1}, respectively. Meanwhile, the H$_2$ evolution rate is up to 28.0 mmol g^{-1} h^{-1} with apparent quantum efficiency of 23.33% at 420 nm in the H$_2$ evolution half reaction. This study provides a new opportunity for constructing a Z-scheme overall water splitting system by exploiting the redox reactions of other metal cation vacancies.

1. Introduction

Along with the rapid development of the economy and society, the dramatically increased global energy consumption makes human face serious energy crisis [1,2]. It is very urgent to develop a novel renewable energy to replace the traditional fossil fuels. As a green sustainable energy, hydrogen possesses several advantages including environmental friendliness and high energy density, both of which meet the requirement of new energy [3,4]. Photocatalytic overall water splitting is considered as the most prospective strategy for hydrogen production, which can directly convert solar energy into chemical energy, thus attracting wide attentions in scientific community [5–7]. Nevertheless, it is severely hampered by the negligible solar to hydrogen conversion efficiency [8,9], owing to the fast recombination rate of photogenerated charge carriers, poor charge separation/transfer efficiency and the reverse reaction of H$_2$/O$_2$ [10,11]. To overcome these challenges, enormous efforts have been devoted to establishing an efficient photocatalytic overall water splitting system [12–17]. Among various strategies, the construction of Z-scheme system has recently attracted much attention [8,18–21].

The Z-scheme system can overcome the drawbacks of a single photocatalyst, which not only extends the light responsive range and promotes the charge separation/transfer efficiency, but also enhances the redox ability, ultimately realizing overall water splitting [22,23]. A typical Z-scheme system is composed of a H$_2$ evolution photocatalyst, an O$_2$ evolution photocatalyst and charge transfer mediator [23–25]. Charge transfer mediator plays a critical role in the successful construction of Z-scheme system, the electrons in the conduction band (CB) of O$_2$ evolution photocatalyst can migrate through the charge transfer mediator to combine with holes in the valence band (VB) of H$_2$ evolution photocatalyst [26]. The charge transfer mediator mainly includes aqueous redox mediator (NO$_3^-$/NO$_2^-$, [Co(bpy)$_3$]$^{3+/2+}$, Fe^{3+}/Fe^{2+}, [Co(phen)$_3$]$^{3+/2+}$ and IO$_3^-$/I$^-$), solid-state electron mediator (noble metal particles and reduced graphene oxide) and the direct ohmic contact between the two photocatalysts [23,27]. Nevertheless, the above three types of charge transfer mediators have their unique weaknesses in the synthesis or photocatalytic reaction process. For aqueous redox mediator, back reactions for the water splitting reaction, reduced light absorption of the photocatalysts, and poor durability are the fatal drawbacks [27]. Choosing solid-state electron mediator as charge transfer mediator or constructing the direct ohmic contact between the two photocatalysts can alleviate the above problems to some extent, but the intimate contact between two components is hard to ensure [24]. Given this, the exploration of an excellent charge transfer

---

mediator for Z-scheme system is urgently required.

Defect engineering of metal oxide has emerged as an effective strategy to generate metal cation vacancies in catalysts. The formation of metal cation vacancies can modify the electronic structure of metal oxide, leading to the variation of the partial valence state, and then forming the defective active sites in metal oxide [28,29]. The redox cycle reaction of other multivalent metal cation is also ubiquity in the reported literatures [29–35], which can be used as a superior charge transfer mediator. More importantly, recent works demonstrate that manganese dioxide (MnO_2) can produce defective Mn^{3+} active sites by intercalating alkaline ions (e.g., H^+, Li^+, Na^+ and K^+) [28,36–43]. To prove this concept, a facile approach is designed to construct a Z-scheme system for overall water splitting by using defect-engineered MnO_2 and monolayer g-C_3N_4 as O_2 and H_2 evolution photocatalyst. The in-situ growth method via a hydrothermal reduction of $KMnO_4$ ensures an intimate contact with g-C_3N_4. Significantly, the defective Mn^{3+} active sites are successfully introduced via defect engineering, which possess the strong adsorption behavior of H_2O and can act as rapid charge transfer due to the redox couples of Mn^{3+}/Mn^{4+}, leading to a superior photocatalytic performance for H_2 evolution and the realization of sustainable overall water splitting.

2. Experimental

2.1. Preparation of samples

Monolayer g-C_3N_4 was prepared according to our previous report [1].

MnO_2/Monolayer g-C_3N_4 composites were fabricated by a in-situ growth method. The typical synthesis process was as follows: Na_2SO_4 (0.02 g) was dissolved in water (15 mL) under sonication. Monolayer g-C_3N_4 (0.1 g) was added to the mixture under sonication for 30 min. Then the aqueous dispersion of $KMnO_4$ (0.302, 0.6041 and 0.906 mL, 30 mg/mL) was added into the solution under magnetic stirring. The mixture was then transferred to a Teflon-lined stainless steel autoclave with a 20 ml capacity and maintained at 160 °C for 6 h. The sample was collected by centrifugal separation and then washed several times with pure water. MnO_2/Monolayer g-C_3N_4 composites were obtained by freeze-drying. The samples with different masses of $KMnO_4$ were denoted as 5%, 10%, and 15% MnO_2/Monolayer g-C_3N_4, respectively. For comparison, Monolayer g-C_3N_4 further reacted by the same synthesis process as the MnO_2/Monolayer g-C_3N_4, the final product was denoted as H-C_3N_4. MnO_2/g-C_3N_4 was also fabricated by the same synthesis process as the MnO_2/Monolayer g-C_3N_4, the only difference was that $Mn(NO_3)_2$ was also selected as the precursor of MnO_2 instead of $KMnO_4$.

## 3. Results and discussion

3.1. Preparation of 2D MnO_2/Monolayer g-C_3N_4 composites

2D MnO_2/Monolayer g-C_3N_4 composites were synthesized through in-situ growth of MnO_2 nanoflower on monolayer g-C_3N_4 matrix, and the typical schematic illustration of the synthesis process is proposed in **Scheme 1**. The surface of monolayer g-C_3N_4 contains abundant hydrophilic functional groups [44], which keeps it highly dispersed in distilled water and makes it act as a surfactant to capture manganese ions homogeneously with multiple adhesion sites, resulting in the intimate contact between MnO_2 and monolayer g-C_3N_4. On the other hand, K^+ can be intercalated between the MnO_2 layer, which leads to partial reduction of Mn^{4+} to Mn^{3+} [28,36–43,45]. We anticipate that the formation of defective Mn^{3+} active sites can promote H_2O adsorption and charge separation/transfer, hence to improve the overall water splitting performance.

Scanning electron microscopy (SEM) image of monolayer g-C_3N_4 (**Fig. 1a**) shows graphite-like layered structure with curled and

wrinkled surface. However, H-C_3N_4 (**Fig. S1a**) displays a multilayer structure, due to the agglomeration during hydrothermal treatment. Meanwhile, **Fig. 1b** and **S1b-c** depict the morphology and microstructure of MnO_2 nanoflower. The SEM image (**Fig. S1b**) demonstrates that the as-prepared MnO_2 nanoflower is built up of uniform flower-like microspheres with a diameter of ca. 1 μm, in which each flower-like microsphere (**Fig. 1b**) consists of many interconnected ultrathin nanosheets. However, each microsphere stands side by side with serious aggregation (**Fig. S1c**). Obviously, both the increase of monolayer g-C_3N_4 thickness and the serious agglomeration of MnO_2 nanoflower go against on their own performance, so exploring a brand new preparation method to overcome the above two disadvantages is very necessary. In our case, the addition of moderate $KMnO_4$ can not only serve as the precursor of MnO_2 nanoflower, but also inhibit the agglomeration of monolayer g-C_3N_4, benefiting from the strong oxidation of $KMnO_4$. The benefits can be intuitively reflected in **Fig. 1c** and **S1d**, MnO_2/Monolayer g-C_3N_4 composites keep the original morphology of monolayer g-C_3N_4 well, and show no agglomeration like H-C_3N_4 during hydrothermal treatment. It can be clearly observed that MnO_2 nanoflower is uniformly dispersed on the surface of monolayer g-C_3N_4 matrix. Most interestingly, the size of MnO_2 nanoflower increases significantly. The homogeneous dispersion and larger size of MnO_2 nanoflower are due to the abundant oxygen functional groups of monolayer g-C_3N_4. **Fig. 1d** shows the HRTEM image of MnO_2/Monolayer g-C_3N_4, the lattice spaces of 0.247 nm and 0.147 nm are attributed to the (111) plane and (311) plane of K^+ intercalated MnO_2 [38], and it is confirmed that MnO_2 and monolayer g-C_3N_4 are in close contact with each other. Additionally, chemical element mapping of MnO_2/Monolayer g-C_3N_4 further demonstrates that the elements C, N, Mn, O and K are homogeneously distributed on the surface of the MnO_2/Monolayer g-C_3N_4 (**Fig. S2**), and also verifies the successful incorporation of K^+ into MnO_2/Monolayer g-C_3N_4. To sum up the above analyses, the conclusions are as followed: $KMnO_4$ and monolayer g-C_3N_4 matrix are complementary to each other. On the one hand, the addition of moderate $KMnO_4$ can effectively inhibit the agglomeration of monolayer g-C_3N_4. On the other hand, monolayer g-C_3N_4 can serve as matrix to dispersedly grow MnO_2 nanoflower and provide abundant oxygen functional groups as nucleation sites of MnO_2 nanoflower. Hence, the intimate contact can be formed, which promotes the charge transfer/separation efficiency, thereby enhancing the corresponding photocatalytic performance.

Next, the X-ray diffraction (XRD), Fourier transform infrared spectroscopy (FT-IR) and X-ray photoelectron spectroscopy (XPS) analyses are examined to further verify the chemical structures of MnO_2/Monolayer g-C_3N_4 composites. As shown in the XRD patterns (**Fig. 2a**), the distinct peak of monolayer g-C_3N_4 centering at 27.4° represents the (002) plane with the stacking of the conjugated aromatic system [21,46,47], which can also be observed evidently in MnO_2/Monolayer g-C_3N_4 composites, indicating that loading MnO_2 does not destroy the fundamental structure of monolayer g-C_3N_4. Meanwhile, MnO_2 nanoflower shows four XRD peaks at 12.1°, 24.2°, 36.7° and 66.0°, which are assigned to the (001), (002), (111) and (311) crystal planes of δ-MnO_2 (JCPDS-80-1098) [43,48]. As the content of MnO_2 increases, the diffraction peaks of MnO_2 appear and strengthen gradually, confirming that the successful preparation of MnO_2/Monolayer g-C_3N_4 composites. The FT-IR spectra of monolayer g-C_3N_4 and MnO_2/Monolayer g-C_3N_4 are displayed in **Fig. 2b**, and no distinct change is found between them. The peak at about 809 cm^{-1} is assigned to the breathing mode of the triazine units [49]. The strong peaks in the range between 1218 to 1662 cm^{-1} are attributed to the CN heterocycles [50], and the broad peak observed between 3000 to 3600 cm^{-1} is considered as the absorbed H_2O molecules and the uncondensed amino groups [51]. The results manifest that the chemical structure of monolayer g-C_3N_4 is maintained well after loading MnO_2.

XPS is further used to verify the successful preparation of MnO_2/Monolayer g-C_3N_4 composites and examine the valence state of Mn element. The survey XPS spectrum (**Fig. 3a**) reveals the existence of C,
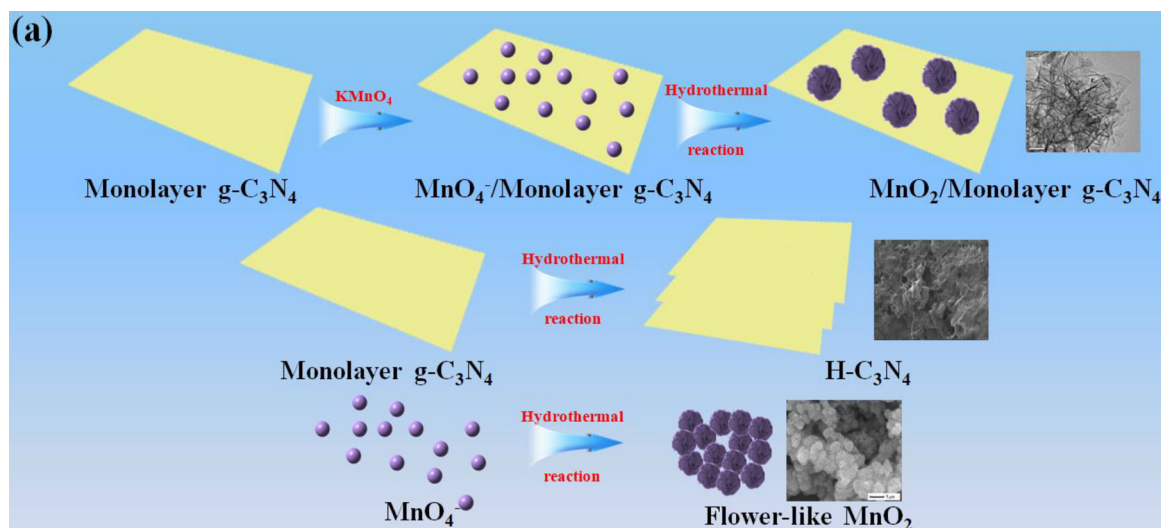
Scheme 1. The formation process of MnO_2/Monolayer g-C_3N_4.

N, Mn and O elements, which means the successful introduction of MnO_2. The corresponding high-resolution spectrum of each element is further studied in **Fig. 3**. The C 1 s spectrum of 10% MnO_2/Monolayer g-C_3N_4 in **Fig. 3b** demonstrates three major peaks. The peaks at 284.5 and 288.2 eV are ascribed to the inherent chemical bonds of monolayer g-C_3N_4, carbon contamination and the typical aromatic C−N≡C co-ordination respectively [52]. While the new peak at 285.8 eV is as-signed to C−O bond, which is combined by C atoms of monolayer g-C_3N_4 and O atoms of MnO_2 nanoflower [53,54]. The formation of C−O bond indicates that monolayer g-C_3N_4 and MnO_2 are not just connected physically, but forming a tight interface for charge migration via C−O bond. There are four peaks at 398.7, 399.7, 401.1 and 404.8 eV re-spectively in the N 1 s spectrum (**Fig. 3c**), which can be attributed to

sp^2-hybridized nitrogen (C═N−C), the tertiary N bonded to carbon atoms N−(C)$_3$ or H−N−(C)$_2$, terminal amino functions (C−N−H), N−H and N═O [55]. **Fig. 3d** shows the high-resolution Mn 2p spectrum, which can be deconvoluted into four peaks. The peaks at 643.4 and 654.9 eV are assigned to Mn^{3+} (2p$_{3/2}$ and 2p$_{1/2}$, respectively), the other two at 642.1 and 653.5 eV correspond to Mn^{4+} (2p$_{3/2}$ and 2p$_{1/2}$, respectively), which confirm the coexistence of Mn^{3+} and Mn^{4+} in MnO_2/Monolayer g-C_3N_4. It is worth noticng that defective Mn^{3+} ac-tive sites pave a pathway for fast charge transfer during the photo-catalytic H$_2$ evolution reaction. The O 1s spectrum of 10% MnO_2/ Monolayer g-C_3N_4 in **Fig. 3e** exhibits three peaks at 530.0, 531.3 and 533.1 eV, which are ascribed to the lattice O atoms of MnO_2, surface adsorbed oxygen and adsorbed molecular water respectively [56]. The
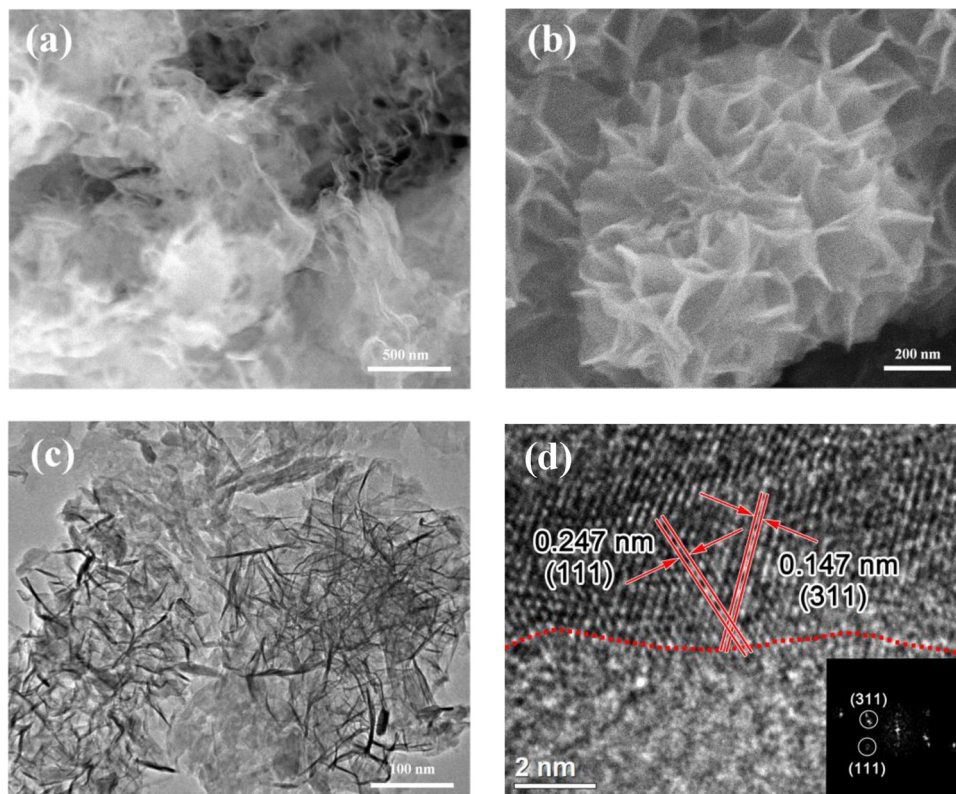
Fig. 1. (a) SEM image of monolayer g-C_3N_4; (b) SEM image of MnO_2 nanoflower; (c) TEM image and (d) HRTEM image of 10% MnO_2/Monolayer g-C_3N_4.
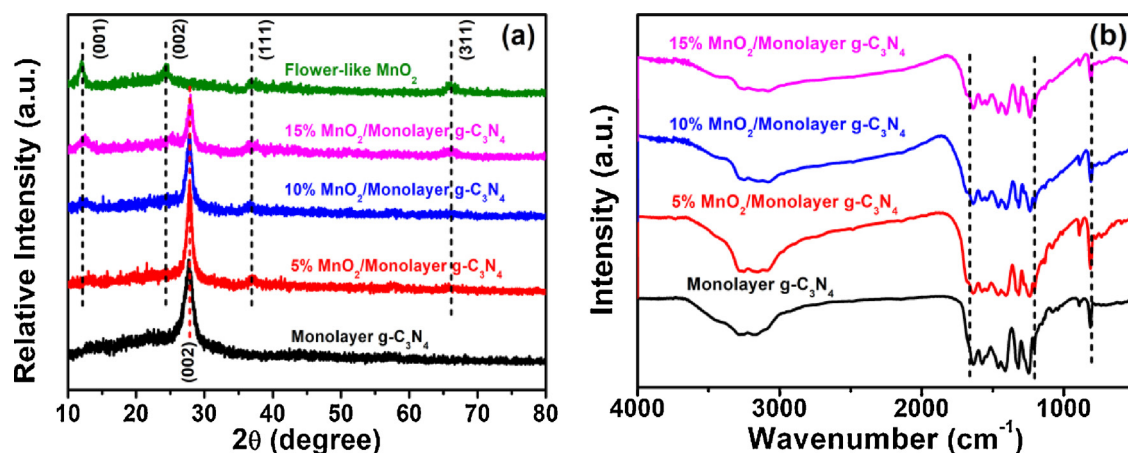
Fig. 2. (a) XRD patterns; (b) FT-IR spectra of the monolayer g-C$_3$N$_4$ and MnO$_2$/Monolayer g-C$_3$N$_4$.

high-resolution K 2p spectrum is shown in **Fig. 3f**, the peaks at 293.0 and 195.4 eV confirm the successful incorporation of K$^+$ into MnO$_2$/Monolayer g-C$_3$N$_4$, which is agreement with the result of the element mapping in **Fig. S2f**. Because of the intercalated K$^+$, the Mn element of MnO$_2$ is not purely +4 oxidation state, part of Mn^{4+} are reduced to Mn^{3+} and the conductivity of MnO$_2$/Monolayer g-C$_3$N$_4$ can be improved [40]. To further investigate the existed defective Mn^{3+} active sites, the electron paramagnetic resonance (EPR) spectrum is carried out. **Fig. S3** shows the EPR spectra of commercial MnO$_2$ and flower-like MnO$_2$. In comparison to commercial MnO$_2$, flower-like MnO$_2$ has a stronger EPR signal, which indicates that the flower-like MnO$_2$ possesses more defective Mn^{3+} active sites. To study the influence of Mn^{3+} defect sites on MnO$_2$ and determine the energy level of defects, the density of states (DOS) are calculated. **Fig. S4** shows that the band gap of commercial MnO$_2$ is 0.67 eV, which is lower than the experiment value because of the known limitation of plain DFT method [57,58]. Compared with commercial MnO$_2$, flower-like MnO$_2$ exhibits enlarged band gap. The VB of flower-like MnO$_2$ is more positive and CB is nearly unchanged, which leads to stronger oxidization ability. **Fig. S4b** shows the energy level of Mn^{3+} defect sites is located at about 0.5 eV. Hence, from the above XRD, FT-IR, XPS, EPR and DOS analyses, it is concluded that MnO$_2$ is incorporated into monolayer g-C$_3$N$_4$ successfully. More importantly, K$^+$ is also intercalated into the layers of MnO$_2$, and the formation of defective Mn^{3+} active sites is verified.

3.2. Photocatalytic performance

In order to characterize the photocatalytic activity of MnO$_2$/Monolayer g-C$_3$N$_4$ composites, H$_2$ evolution from water was carried out under visible light irradiation. In this photocatalytic process, triethanolamine (TEOA) is chosen as the hole sacrificial reagent, because TEOA is the most suitable sacrificial reagents for g-C$_3$N$_4$-based photocatalyst [59]. As displayed in **Fig. 4a**, monolayer g-C$_3$N$_4$ exhibits a moderate H$_2$ evolution rate (18.6 mmol g^{-1} h^{-1}) after loading 3 wt.% Pt co-catalyst. However, H$_2$ evolution activity of H-C$_3$N$_4$ is only 10.1 mmol g^{-1} h^{-1}, which is clearly lower than that of monolayer g-C$_3$N$_4$ due to the effect of agglomeration. Note that the MnO$_2$ nanoflower is catalytic inert for H$_2$ evolution, mainly owing to its unsuitable CB potential. Surprisingly, embedding a small amount of MnO$_2$ nanoflower into monolayer g-C$_3$N$_4$ can significantly improve the H$_2$ evolution activity. The highest H$_2$ evolution rate is observed on 10% MnO$_2$/Monolayer g-C$_3$N$_4$ (28.0 mmol g^{-1} h^{-1}). More loading amounts of MnO$_2$ (15%) results in decreased performance, indicating that the photocatalytic activity of MnO$_2$/Monolayer g-C$_3$N$_4$ composite is tightly related to the contents of MnO$_2$. An appropriate content of MnO$_2$ contributes to charge separation and transport, thereby obtaining the optimal photocatalytic activity. However, More loading amounts of

MnO$_2$ (15%) results in decreased performance, indicating that the photocatalytic activity of MnO$_2$/Monolayer g-C$_3$N$_4$ composite is tightly related to the contents of MnO$_2$. An appropriate content of MnO$_2$ contributes to charge separation and transport, thereby obtaining the optimal photocatalytic activity. However, the excess amount of MnO$_2$ would cover the surface of monolayer g-C$_3$N$_4$, which may weaken the light adsorption capability of monolayer g-C$_3$N$_4$ and therefore limits the generation of electrons from monolayer g-C$_3$N$_4$ [60–63]. Correspondingly, due to the decrease of the VB holes of monolayer g-C$_3$N$_4$, the excited electrons in the CB of MnO$_2$ can't be consumed in time and recombine with the photoinduced holes in the VB of MnO$_2$ again. Therefore excess amount of MnO$_2$ would become the recombination sites of photogenerated charge carriers, and which ultimately leads to decline of photocatalytic performance. In order to verify the importance of abundant defective Mn^{3+} active sites for photocatalytic performance, Mn(NO$_3$)$_2$ is selected as the precursor of MnO$_2$ to prepare MnO$_2$/g-C$_3$N$_4$ composite, which shows a lower H$_2$ evolution rate of 12.9 mmol g^{-1} h^{-1} as compared to monolayer g-C$_3$N$_4$ and the composite prepared by KMnO$_4$ (**Fig. S5**). For analyzing the reason of decreased activity, SEM, TEM and XPS are employed to investigate the morphology of MnO$_2$ in MnO$_2$/g-C$_3$N$_4$ prepared by using Mn(NO$_3$)$_2$ as the precursor of MnO$_2$. First, XPS analysis is performed to investigate the chemical state in MnO$_2$/g-C$_3$N$_4$ prepared by using Mn(NO$_3$)$_2$ as the precursor. As shown in **Fig. S6**, the high-resolution Mn 2p spectrum of MnO$_2$/g-C$_3$N$_4$ can also be deconvoluted into Mn^{3+} and Mn^{4+} species, but MnO$_2$/g-C$_3$N$_4$ possesses significantly less Mn^{3+} than MnO$_2$/Monolayer g-C$_3$N$_4$, suggesting that more defective Mn^{3+} active sites are more conducive to photocatalytic activity [45]. As shown in the SEM and TEM images (**Fig. S7a-b**), the irregular MnO$_2$ nanoparticles with size about 150 nm are anchored on g-C$_3$N$_4$, which is unable to form the intimate interface between MnO$_2$ and g-C$_3$N$_4$ like 2D/2D MnO$_2$/Monolayer g-C$_3$N$_4$ [18]. And at the same time, monolayer g-C$_3$N$_4$ exists obvious aggregation in MnO$_2$/g-C$_3$N$_4$ photocatalyst, which can also cause apparent decrease of the photocatalytic activity. This therefore implied that using KMnO$_4$ as the precursor can form the intimate interface between MnO$_2$ and monolayer g-C$_3$N$_4$, inhibit the agglomeration of monolayer g-C$_3$N$_4$ and boost the formation of defective Mn^{3+} active sites to effectively facilitate the charge separation/transfer, thereby enhancing the photocatalytic activity.

The cycled experiments of photocatalytic H$_2$ evolution are carried out to test the stability and recyclability of 10% MnO$_2$/Monolayer g-C$_3$N$_4$. As shown in **Fig. 4b**, the continuing decrease of H$_2$ evolution rate is observed, it might be due to the ongoing draining of TEOA. After adding 5 mL TEOA into reaction solution, the H$_2$ evolution rate recovers to the initial value, which also suggests that the decrease of H$_2$ evolution rate can be ascribed to the consumption of TEOA. In addition, the huge consumption of TEOA also further suggests the superior
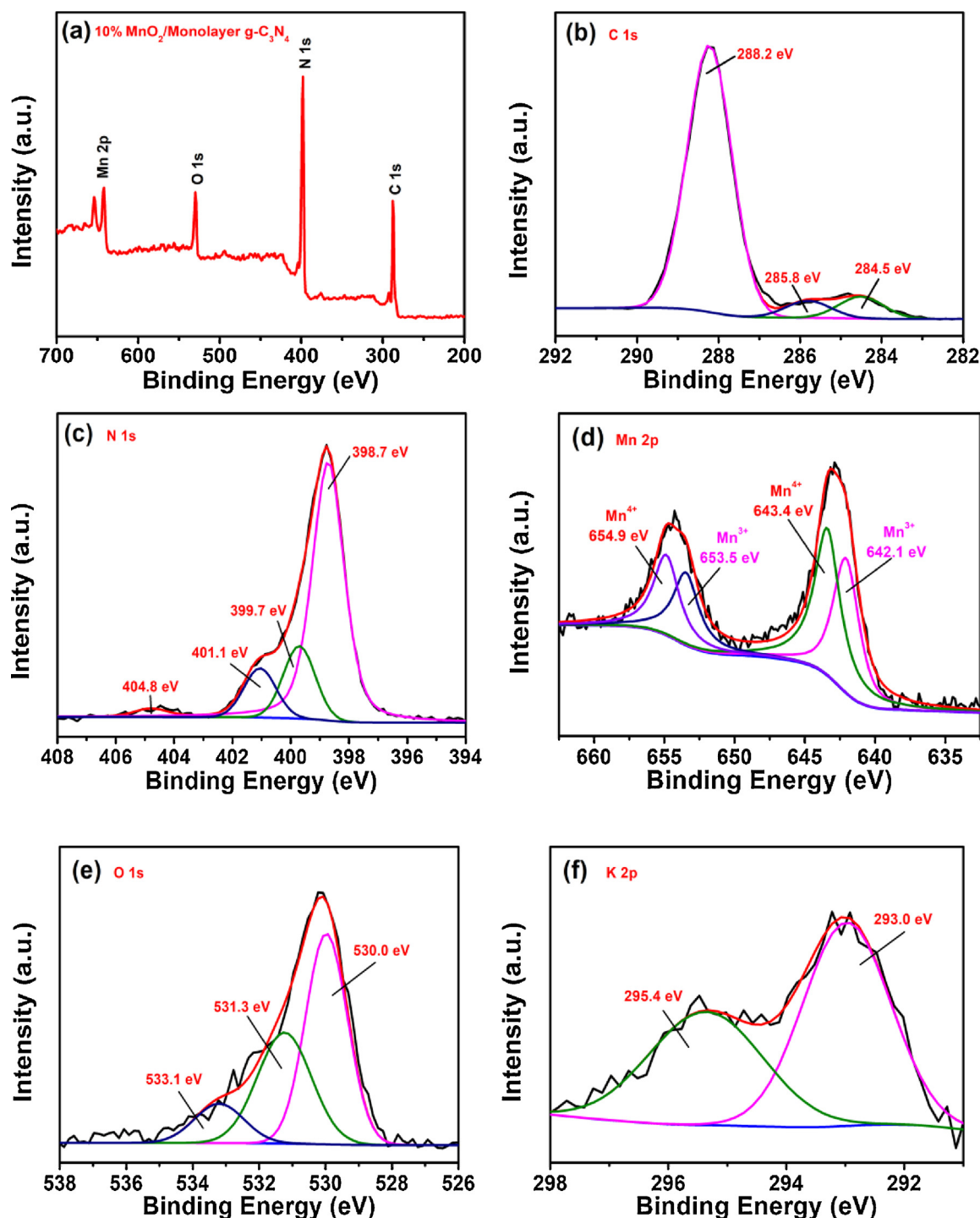
Fig. 3. XPS spectra of the 10% MnO_2/Monolayer g-C_3N_4 (a) Survey; (b) C 1 s; (c) N 1 s; (d) Mn 2p; (e) O1 s and (f) K 2p.

photocatalytic performance. **Fig. 4c** shows the apparent quantum efficiency (AQE) for 10% MnO_2/Monolayer g-C_3N_4 under different monochromatic light irradiation. The calculated AQE value at 420 nm comes up to 23.33%, and decreases to 9.49%, 1.04% and 0% at 435 nm, 450 nm and 550 nm, which exceed most of the g-C_3N_4-based photocatalysts (**Table S2**).

In view of the above half reaction of H_2 evolution, 10% MnO_2/Monolayer g-C_3N_4 is chosen to evaluate overall water splitting performance in pure water without any sacrificial reagents under visible light ($\lambda > 400$ nm) irradiation. Notably, the simultaneous and steady evolution of H_2 and O_2 in a nearly molar ratio of 2:1 (60.6 and

28.9 $\mu mol\, g^{-1}\, h^{-1}$) can be observed in **Fig. 4d**, which indicates that overall water splitting can indeed happen. The photocatalytic performance is better than most of the g-C_3N_4-based photocatalysts (**Table S3**). At the same time, the photocatalytic activity displays any obvious decay in a 20 h reaction, suggesting the excellent stability and durability of photocatalyst.

3.3. Possible photocatalytic mechanism

The photocatalytic activity depends on the following three aspects: light absorption, charge separation/transfer and surface redox reaction.
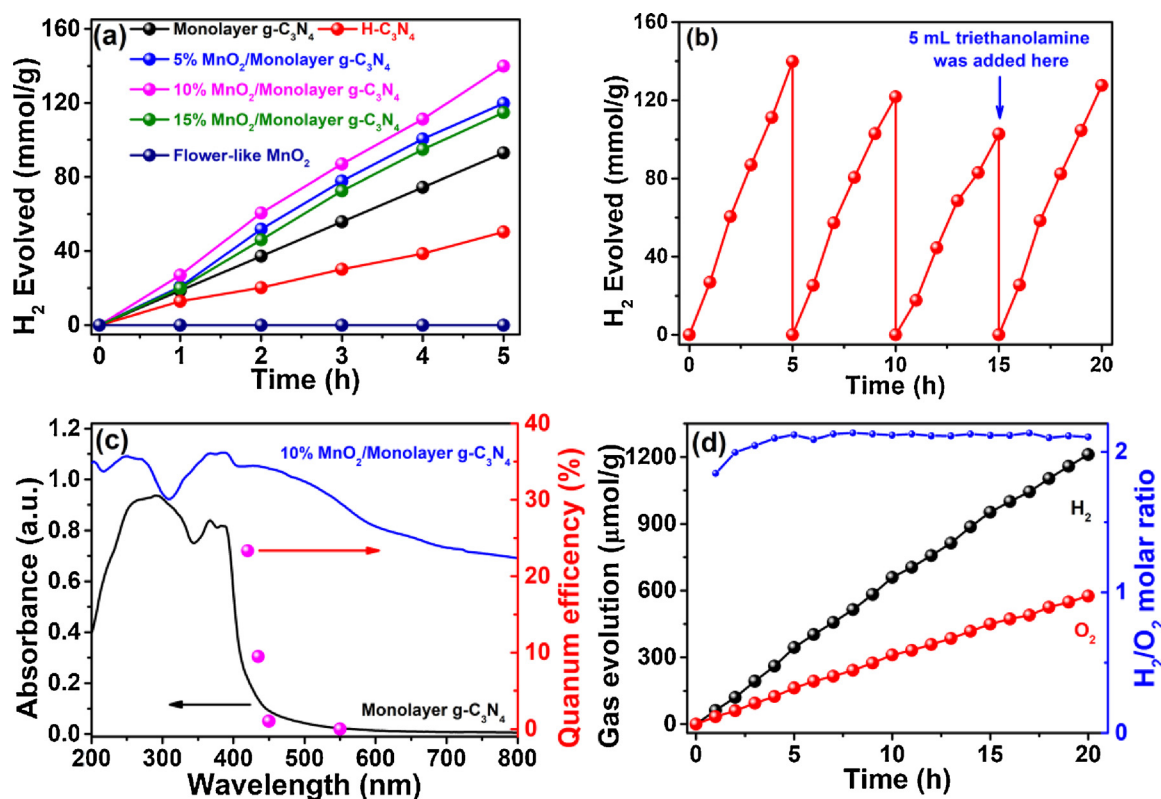
Fig. 4. (a) Photocatalytic H_2 evolution over the as-prepared samples under visible light irradiation, using Pt (3%) as a co-catalytst; (b) photocatalytic stability of 10% MnO_2/Monolayer g-C_3N_4; (c) Wavelength dependence of external quantum efficiency for 10% MnO_2/Monolayer g-C_3N_4; (d) The overall water spitting performance of 10% MnO_2/Monolayer g-C_3N_4 under visible light irradiation, using Pt (3%) as a co-catalytst.

The optical properties of MnO_2/Monolayer g-C_3N_4 composites are investigated by UV–vis diffuse reflectance spectra (**Fig. 5a**). As expected, compared to monolayer g-C_3N_4, all the MnO_2/Monolayer g-C_3N_4 composites display remarkably enhanced light absorption within the whole light range with increasing MnO_2 amounts. This benefits from the intrinsic absorption of dark-colored MnO_2, and consequently enhances the photocatalytic activity of MnO_2/Monolayer g-C_3N_4 composites significantly.

Moreover, photoluminescence (PL) spectra and photoelectrochemical measurement are explored to investigate the charge transfer efficiency under visible light irradiation [64]. As shown in **Fig. 5b**, the main emission peak for monolayer g-C_3N_4 and MnO_2/Monolayer g-C_3N_4 composites is centered at 450 nm, which corresponds well to the absorption edge of monolayer g-C_3N_4. The high emission intensity of monolayer g-C_3N_4 indicates the fast recombination rate of photogenerated charge carriers. When monolayer g-C_3N_4 couples with MnO_2 nanoflower, the emission intensities of MnO_2/Monolayer g-C_3N_4 composites all obviously decrease, implying that the successful introduction of MnO_2 with defective Mn^{3+} active sites can inhibit the recombination of photogenerated charge carriers effectively. **Fig. 5c** makes comparison of the photocurrent response of monolayer g-C_3N_4 and MnO_2/Monolayer g-C_3N_4 composites on a typical switch on-off cycles. All the composites exhibit a higher current density than that of monolayer g-C_3N_4, which demonstrates that composites possess superior charge separation efficiency than monolayer g-C_3N_4. Especially, 10% MnO_2/Monolayer g-C_3N_4 shows the highest current density, which is about 4.0 times higher than that of monolayer g-C_3N_4. The results correspond to the enhanced photocatalytic activity of 10% MnO_2/Monolayer g-C_3N_4. Furthermore, the same results in **Fig. 5d** are obtained by the electrochemical impedance spectroscopy (EIS). Clearly, the MnO_2/Monolayer g-C_3N_4 composites exhibit a smaller radius than that of monolayer g-C_3N_4, suggesting that the successful construction of MnO_2/Monolayer g-C_3N_4 with defective Mn^{3+} active sites induces the

decrease of the charge transfer resistance, thus facilitating more effective charge separation and transport. Based on above photoelectrochemical measurements, it can be concluded that MnO_2 doping promotes the capacity of light absorption, and the defective Mn^{3+} active sites between MnO_2 and monolayer g-C_3N_4 facilitate the efficient charge separation/transfer by following the redox cycle between Mn^{3+} and Mn^{4+}, thus accelerating the process of photocatalytic water splitting. In order to elucidate the Z-scheme mechanism, the detailed band structure/position of MnO_2/Monolayer g-C_3N_4 is investigated by UV–vis diffuse reflectance spectra and the valence band X-ray photoelectron spectroscopy (VB XPS). According to UV–vis diffuse reflectance spectra in **Fig. S8**, The corresponding band gaps (E_g) of monolayer g-C_3N_4 and MnO_2 are estimated to be 2.92 and 1.64 eV, respectively. As shown in **Fig. S9**, the VB maximum potential (E_{VB}) of monolayer g-C_3N_4 is calculated to be 2.34 eV through VB XPS. According to the formula ($E_{NHE}/V = \Phi + 2.34\,eV - 4.44$, where E_{NHE} is potential of normal hydrogen electrode and Φ of 3.88 eV is the electron work function of the analyzer) [65], the contact potential difference between the sample and the analyzer is estimated to be 1.78 V. the CB potential (E_{CB}) of MnO_2 is estimated to be 0.64 V by the equations ($E_{CB} = X - E_e - 0.5\,E_g$, where X of 5.96 eV is absolute electronegativity and E_e of 4.5 eV is the free energy of electrons of the semiconductor on the hydrogen scale) [21,66]. According to $E_{CB} = E_{VB} - E_g$, E_{CB} of monolayer g-C_3N_4 and E_{VB} of MnO_2 can be calculated to be -1.14 and 2.28 V, respectively. The band alignment of MnO_2/Monolayer g-C_3N_4 for photocatalytic water splitting is illustrated in **Fig. 6a**, monolayer g-C_3N_4 and MnO_2 are responsible for one half-reaction, respectively. Moreover, the defective Mn^{3+} active sites can serve as the electron transport chain between the above two photocatalysts to construct a Z-scheme photocatalytic water splitting system. Upon visible light irradiation, the photogenerated electron-hole pairs of monolayer g-C_3N_4 and MnO_2 are both separated. Presumably due to the existence of defective Mn^{3+} active sites and the appropriate redox potential of Mn^{4+}/Mn^{3+} (+1.06 V) [26,67], which
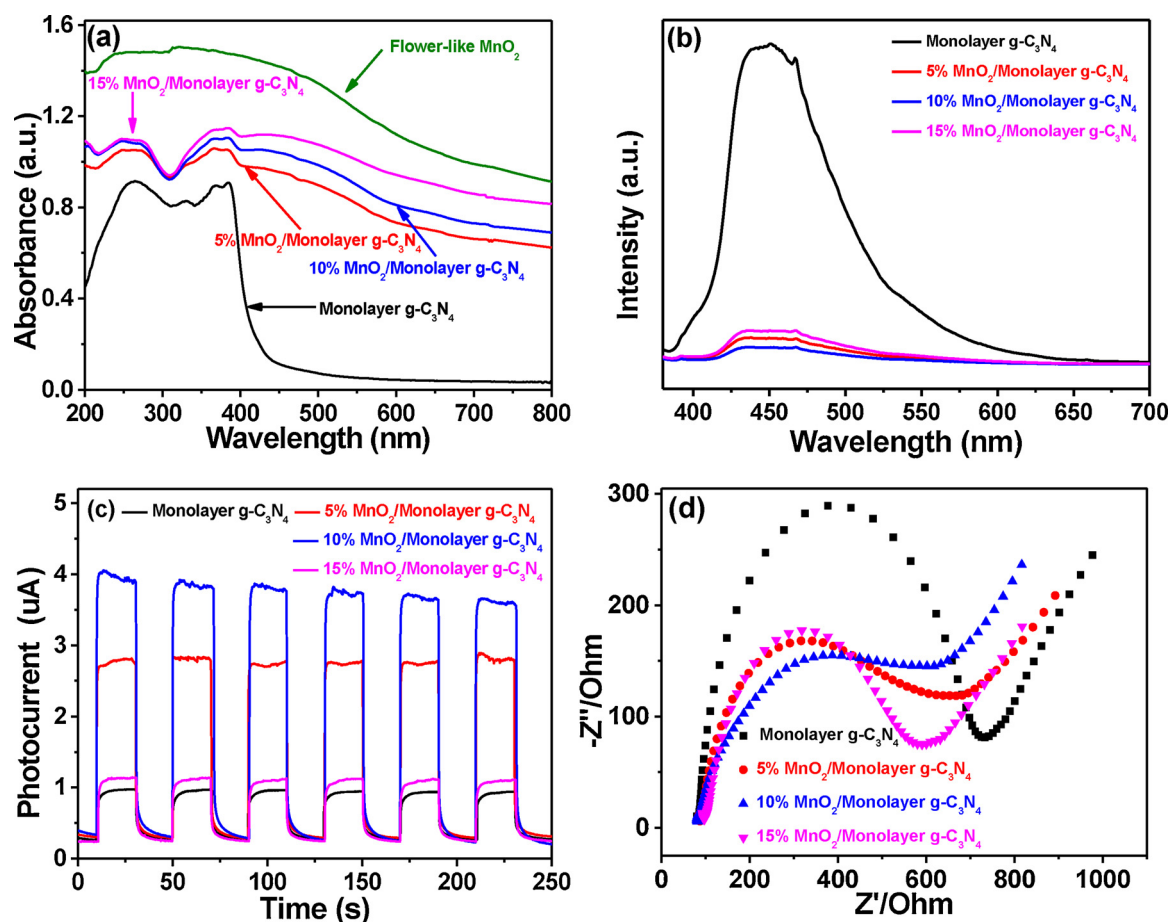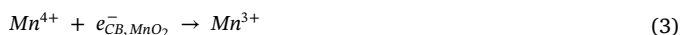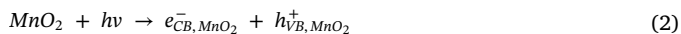
Fig. 5. (a) Optical absorption spectroscopy; (b) The PL spectra; (c) Photocurrent responses; (d) ESI Nyquist plots of the monolayer g-C_3N_4 and MnO_2/Monolayer g-C_3N_4.

is positive enough for the CB electrons of MnO_2, so the excited electrons in the CB of MnO_2 can be trapped to reduce Mn^{4+} into Mn^{3+}, and then Mn^{3+} is converted to Mn^{4+} again by the photoinduced holes in the VB of monolayer g-C_3N_4. Such redox cycle Mn^{4+}/Mn^{3+} can lead to more effective charge separation/transfer. In addition, the excited electrons in the CB of monolayer g-C_3N_4 react with H^+ to produce H_2 and the photoinduced holes in the VB of MnO_2 participate in O_2 evolution reaction or TEOA oxidation. The above analysis implies that the cycle reaction of Mn^{4+}/Mn^{3+} maybe do exist, and the possible main reactions are listed as follows:

$$C_3N_4 \;+\; h\nu \;\rightarrow\; e^-_{CB,C_3N_4} \;+\; h^+_{VB,C_3N_4} \tag{1}$$

$$MnO_2 \;+\; h\nu \;\rightarrow\; e^-_{CB,MnO_2} \;+\; h^+_{VB,MnO_2} \tag{2}$$

$$Mn^{4+} \;+\; e^-_{CB,MnO_2} \;\rightarrow\; Mn^{3+} \tag{3}$$

$$Mn^{3+} \;+\; h^+_{VB,C_3N_4} \;\rightarrow\; Mn^{4+} \tag{4}$$

$$2H^+ \;+\; 2e^-_{CB,C_3N_4} \;\rightarrow\; H_2 \tag{5}$$

$$2H_2O \;+\; 4h^+_{VB,MnO_2} \;\rightarrow\; O_2 \;+\; 4H^+ \tag{6}$$

Additionally, the evidence is necessary to prove the existence of Mn^{4+}/Mn^{3+} redox cycle reaction. And according to previous research, the XPS analysis is a common and effective method [32,68–70], the high-resolution Mn 2p spectrum before and after photocatalytic reaction is shown in **Fig. S10**. The Mn element still maintains the coexistence of Mn^{4+} and Mn^{3+} species with just a slight decrease of Mn^{3+} species in MnO_2/Monolayer g-C_3N_4 after a 20 h photocatalytic reaction, which implies that the Mn^{4+}/Mn^{3+} redox cycle reaction may indeed

exist.

To validate the above hypothesis about the Z-scheme charge separation process, the electron spinresonance (ESR) analysis in **Fig. 6c-d** is performed to reveal the main active oxygen species in the photocatalytic process [21,71–73]. For MnO_2 nanoflower, there is no ESR signal in the dark, while the obvious characteristic peaks of hydroxyl radicals (˙OH) are observed and no signals of superoxide radicals (O_2˙$^-$) are detected under visible light irradiation. Meanwhile, the obvious signal of O_2˙$^-$ can be observed for monolayer g-C_3N_4, and no obvious signal of ˙OH can be detected regardless in the dark or under visible light irradiation. More importantly, when choosing MnO_2/Monolayer g-C_3N_4 as the photocatalyst, O_2˙$^-$ and ˙OH signals are simultaneously detected under visible light irradiation. The above ESR analysis manifests that the successful construction of Z-scheme system in MnO_2/Monolayer g-C_3N_4 composite rather than the traditional type II structure. In detail, if MnO_2/Monolayer g-C_3N_4 composite follows the traditional type II structure, the photoinduced electrons on the CB of monolayer g-C_3N_4 may transfer to the CB of MnO_2, and the photoinduced holes on the VB of MnO_2 should flow to the VB of monolayer g-C_3N_4. However, the CB edge potential of MnO_2 is lower than the standard redox potential of the O_2/O_2˙$^-$ (-0.046 V vs NHE, pH = 7) [21,74], and therefore the electrons on the VB of MnO_2 cannot reduce the O_2 to generate O_2˙$^-$. The VB edge potential of monolayer g-C_3N_4 is not deep enough to generate ˙OH, because the VB edge potential is more positive than the standard redox potential of the OH$^-$/˙OH (1.99 V vs NHE, pH = 7) and H_2O/˙OH (2.34 V vs NHE, pH = 7) [21,75]. Obviously, the above analysis is entirely against the ESR analysis. Therefore, it can be concluded that Z-scheme charge transfer is successfully integrated in MnO_2/Monolayer g-C_3N_4 due to the valence
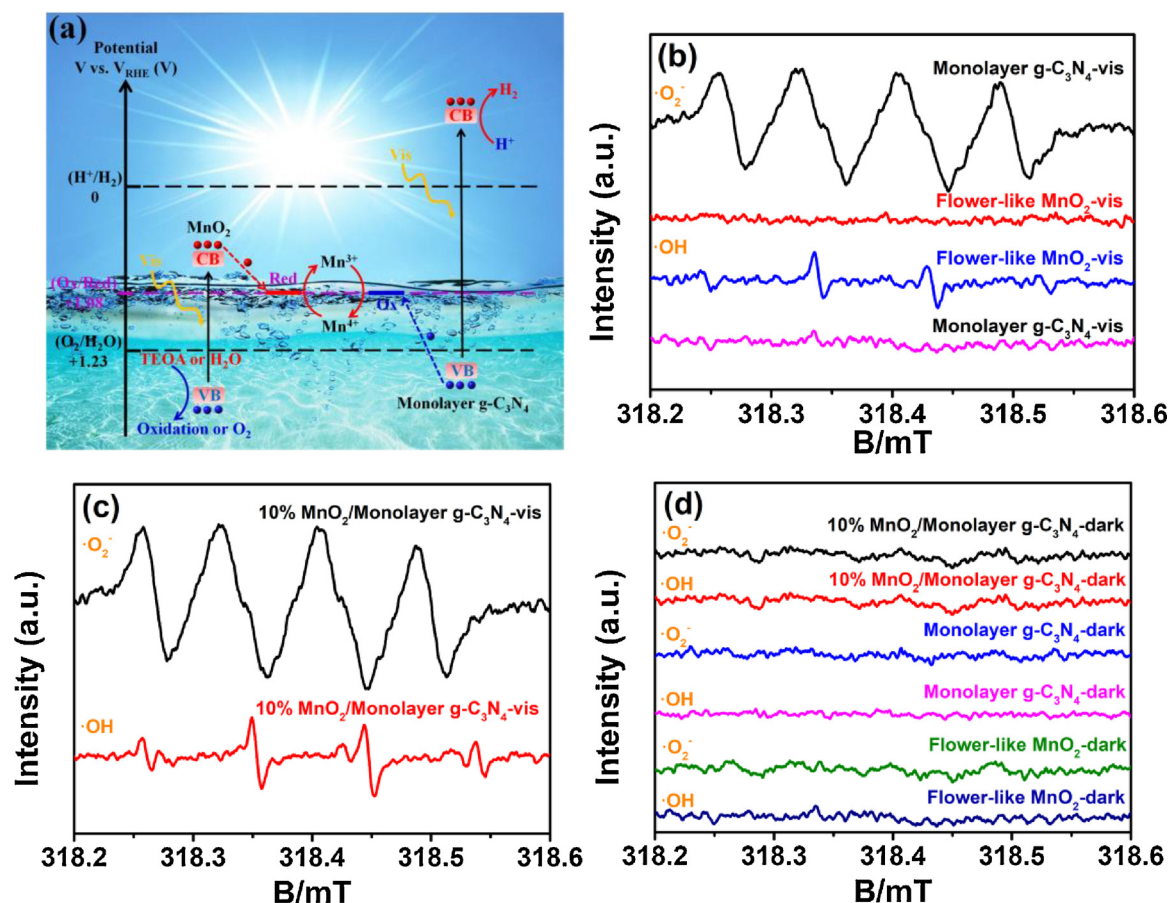
Fig. 6. (a) Z-Scheme charge transfer mechanism diagram of MnO_2/Monolayer $g-C_3N_4$; (b) DMPO spin-trapping ESR spectra of MnO_2 nanoflower, monolayer $g-C_3N_4$ and 10% MnO_2/Monolayer $g-C_3N_4$ (in aqueous for DMPO-·OH, in methanol for DMPO-$O_2^{·-}$); (d) DMPO spin-trapping ESR spectra of MnO_2 nanoflower, monolayer $g-C_3N_4$ and 10% MnO_2/Monolayer $g-C_3N_4$ without light irradiation.

change between Mn^{3+} and Mn^{4+}, which enables the photocatalyst a greatly improved charge separation/transfer efficiency, leading to a promoted photocatalytic activity for H_2 evolution and the realization of overall water splitting performance.

4. Conclusions

In summary, a Z-scheme photocatalyst was successfully synthesized through *in-situ* embedding MnO_2 nanoflower into monolayer $g-C_3N_4$ matrix. This study highlights that the obtained composite possesses partial defective Mn^{3+} active sites, which can promote H_2O adsorption and induce Z-scheme charge transfer by following the redox cycle between Mn^{3+} and Mn^{4+}, leading to excellent overall water splitting performance. Moreover, the composite exhibits significantly enhanced H_2 evolution activity with a notable quantum efficiency of 23.33% at 420 nm. The findings provide a successful paradigm for utilizing the valence change of self-doped metal ion to achieve overall water splitting.

Acknowledgements

Appendix A. Supplementary data

Supplementary material related to this article can be found, in the online version, at doi:https://doi.org/10.1016/j.apcatb.2018.08.073.

References

[1] N. Tian, Y. Zhang, X. Li, K. Xiao, X. Du, F. Dong, G.I.N. Waterhouse, T. Zhang, H. Huang, Nano Energy 38 (2017) 72–81.
[2] P. Xia, B. Zhu, J. Yu, S. Cao, M. Jaroniec, J. Mater. Chem. A 5 (2017) 3230–3238.
[3] Z.A.L.G.G. Zhang, X.C. Wang, Angew. Chem. Int. Ed. 55 (2016) 15712–15727.
[4] H. Xu, J. Yi, X. She, Q. Liu, L. Song, S. Chen, Y. Yang, Y. Song, R. Vajtai, J. Lou, H. Li, S. Yuan, J. Wu, P.M. Ajayan, Appl. Catal. B 220 (2018) 379–385.
[5] D. Zheng, X.N. Cao, X. Wang, Angew. Chem. Int. Ed. 55 (2016) 11512–11516.
[6] G. Li, J. Shi, G. Zhang, Y. Fang, M. Anpo, X. Wang, Res. Chem. Intermed. 43 (2017) 5137–5152.
[7] J. Yi, X. She, Y. Song, M. Mao, K. Xia, Y. Xu, Z. Mo, J. Wu, H. Xu, H. Li, Chem. Eng. J. 335 (2018) 282–289.
[8] Q. Xu, L. Zhang, J. Yu, S. Wageh, A.A. Al-Ghamdi, M. Jaroniec, Mater. Today (2018).
[9] W. Che, W. Cheng, T. Yao, F. Tang, W. Liu, H. Su, Y. Huang, Q. Liu, J. Liu, F. Hu, Z. Pan, Z. Sun, S. Wei, J. Am. Chem. Soc. 139 (2017) 3021–3026.
[10] M.A. Melo, Z. Wu, B.A. Nail, A.T. De Denko, A.F. Nogueira, F.E. Osterloh, Nano Lett. 18 (2018) 805–810.
[11] L. Yuan, C. Han, M.-Q. Yang, Y.-J. Xu, Int. Rev. Phys. Chem. 35 (2016) 1–36.
[12] G. Zhang, Z.A. Lan, X. Wang, Chem. Sci. 8 (2017) 5261–5274.
[13] L. Gao, Y. Li, J. Ren, S. Wang, R. Wang, G. Fu, Y. Hu, Appl. Catal. B 202 (2017) 127–133.
[14] J. Yan, H. Wu, H. Chen, Y. Zhang, F. Zhang, S.F. Liu, Appl. Catal. B 191 (2016) 130–137.
[15] Q. Zhang, Z. Li, S. Wang, R. Li, X. Zhang, Z. Liang, H. Han, S. Liao, C. Li, ACS Catal. 6 (2016) 2182–2191.
[16] Y. An, Y. Liu, P. An, J. Dong, B. Xu, Y. Dai, X. Qin, X. Zhang, M.H. Whangbo, B. Huang, Angew. Chem. Int. Ed. 56 (2017) 3036–3040.
[17] M.G. Kibria, R. Qiao, W. Yang, I. Boukahil, X. Kong, F.A. Chowdhury, M.L. Trudeau, W. Ji, H. Guo, F.J. Himpsel, L. Vayssieres, Z. Mi, Adv. Mater. 28 (2016) 8388–8397.

[18] T. Su, Q. Shao, Z. Qin, Z. Guo, Z. Wu, ACS Catal. 8 (2018) 2253–2276.
[19] D.J. Martin, P.J. Reardon, S.J. Moniz, J. Tang, J. Am. Chem. Soc. 136 (2014) 12568–12571.
[20] S. Chen, T. Takata, K. Domen, Nat. Rev. Mater. 2 (2017) 17050.
[21] X. She, J. Wu, H. Xu, J. Zhong, Y. Wang, Y. Song, K. Nie, Y. Liu, Y. Yang, M.-T.F. Rodrigues, R. Vajtai, J. Lou, D. Du, H. Li, P.M. Ajayan, Adv. Energy Mater. 7 (2017) 1700025.
[22] Z. Zhang, J. Huang, Y. Fang, M. Zhang, K. Liu, B. Dong, Adv. Mater. 29 (2017) 1606688.
[23] J.W. Fu, J.G. Yu, C.J. Jiang, B. Cheng, Adv. Energy Mater. 8 (2018) 1701503.
[24] S. Chen, T. Takata, K. Domen, Nat. Rev. Mater. 2 (2017) 17050.
[25] X. Wang, ChemSusChem 11 (2018) 327–329.
[26] Y. Wang, H. Suzuki, J. Xie, O. Tomita, D.J. Martin, M. Higashi, D. Kong, R. Abe, J. Tang, Chem. Rev. (2018).
[27] H. Li, W. Tu, Y. Zhou, Z. Zou, Adv. Sci. 3 (2016) 1500389.
[28] Y. Zhao, C. Chang, F. Teng, Y. Zhao, G. Chen, R. Shi, G.I.N. Waterhouse, W. Huang, T. Zhang, Adv. Energy Mater. 7 (2017) 1700005.
[29] Z. Dai, F. Qin, H. Zhao, J. Ding, Y. Liu, R. Chen, ACS Catal. 6 (2016) 3180–3192.
[30] Z. Luo, A.S. Poyraz, C.-H. Kuo, R. Miao, Y. Meng, S.-Y. Chen, T. Jiang, C. Wenos, S.L. Suib, Chem. Mater. 27 (2014) 6–17.
[31] M. Li, L. Zhang, M. Wu, Y. Du, X. Fan, M. Wang, L. Zhang, Q. Kong, J. Shi, Nano Energy 19 (2016) 145–155.
[32] S. Gu, W. Li, F. Wang, S. Wang, H. Zhou, H. Li, Appl. Catal. B 170-171 (2015) 186–194.
[33] H. Li, W. Li, F. Wang, X. Liu, C. Ren, Appl. Catal. B 217 (2017) 378–387.
[34] J. Zhou, A. Zhou, L. Shu, M.-C. Liu, Y. Dou, J.-R. Li, Appl. Catal. B 226 (2018) 421–428.
[35] Y. Yang, P. Gao, X. Ren, L. Sha, P. Yang, J. Zhang, Y. Chen, L. Yang, Appl. Catal. B 218 (2017) 751–757.
[36] N. Jabeen, A. Hussain, Q. Xia, S. Sun, J. Zhu, H. Xia, Adv. Mater. 29 (2017) 1700804.
[37] H. Wang, J. Zhang, X. Hang, X. Zhang, J. Xie, B. Pan, Y. Xie, Angew. Chem. Int. Ed. 54 (2015) 1195–1199.
[38] T. Takashima, K. Hashimoto, R. Nakamura, J. Am. Chem. Soc. 134 (2012) 1519–1527.
[39] K. Jin, H. Seo, T. Hayashi, M. Balamurugan, D. Jeong, Y.K. Go, J.S. Hong, K.H. Cho, H. Kakizaki, N. Bonnet-Mercier, M.G. Kim, S.H. Kim, R. Nakamura, K.T. Nam, J. Am. Chem. Soc. 139 (2017) 2277–2285.
[40] Y.F. Li, S.C. Zhu, Z.P. Liu, J. Am. Chem. Soc. 138 (2016) 5371–5379.
[41] Y. Meng, W. Song, H. Huang, Z. Ren, S.Y. Chen, S.L. Suib, J. Am. Chem. Soc. 136 (2014) 11452–11464.
[42] S. Kim, K.W. Nam, S. Lee, W. Cho, J.S. Kim, B.G. Kim, Y. Oshima, J.S. Kim, S.G. Doo, H. Chang, D. Aurbach, J.W. Choi, Angew. Chem. Int. Ed. 54 (2015) 15094–15099.
[43] M. Yeager, W. Du, R. Si, D. Su, N. Marinković, X. Teng, J. Phys. Chem. C 116 (2012) 20173–20181.
[44] X. She, J. Wu, J. Zhong, H. Xu, Y. Yang, R. Vajtai, J. Lou, Y. Liu, D. Du, H. Li, P.M. Ajayan, Nano Energy 27 (2016) 138–146.
[45] W. Yang, Y. Zhu, F. You, L. Yan, Y. Ma, C. Lu, P. Gao, Q. Hao, W. Li, Appl. Catal. B 233 (2018) 184–193.
[46] H. Ou, L. Lin, Y. Zheng, P. Yang, Y. Fang, X. Wang, Adv. Mater. (2017) 29.
[47] X. Wang, Y. Liang, W. An, J. Hu, Y. Zhu, W. Cui, Appl. Catal. B 219 (2017) 53–62.
[48] V.B.R. Boppana, S. Yusuf, G.S. Hutchings, F. Jiao, Adv. Funct. Mater. 23 (2013) 878–884.
[49] P. Yan, D. Jiang, Y. Tian, L. Xu, J. Qian, H. Li, J. Xia, H. Li, Biosens. Bioelectron. 111 (2018) 74–81.
[50] Z. Mo, X. She, Y. Li, L. Liu, L. Huang, Z. Chen, Q. Zhang, H. Xu, H. Li, RSC Adv. 5 (2015) 101552–101562.
[51] X. She, J. Wu, H. Xu, Z. Mo, J. Lian, Y. Song, L. Liu, D. Du, H. Li, Appl. Catal. B 202 (2017) 112–117.
[52] X. Zhu, J. Liu, Z. Zhao, J. Yan, Y. Xu, Y. Song, H. Ji, H. Xu, H. Li, RSC Adv. 7 (2017) 38682–38690.
[53] M. Wang, M. Shen, L. Zhang, J. Tian, X. Jin, Y. Zhou, J. Shi, Carbon 120 (2017) 23–31.
[54] J. Liu, N.Y. Liu, H. Li, L.P. Wang, X.Q. Wu, H. Huang, Y. Liu, F. Bao, Y. Lifshitz, S.T. Lee, Z.H. Kang, Nanoscale 8 (2016) 11956–11961.
[55] X. She, L. Liu, H. Ji, Z. Mo, Y. Li, L. Huang, D. Du, H. Xu, H. Li, Appl. Catal. B 187 (2016) 144–153.
[56] V.P. Santos, M.F.R. Pereira, J.J.M. Órfão, J.L. Figueiredo, Appl. Catal. B 99 (2010) 353–363.
[57] T. Xiong, H. Wang, Y. Zhou, Y. Sun, W. Cen, H. Huang, Y. Zhang, F. Dong, Nanoscale 10 (2018) 8066–8074.
[58] M. Li, J. Zhang, W. Dang, S.K. Cushing, D. Guo, N. Wu, P. Yin, Phys. Chem. Chem. Phys. 15 (2013) 16220–16226.
[59] M. Wang, S. Shen, L. Li, Z. Tang, J. Yang, J. Mater. Sci. 52 (2017) 5155–5164.
[60] M. Zhou, S. Wang, P. Yang, C. Huang, X. Wang, ACS Catal. 8 (2018) 4928–4936.
[61] C. Li, S. Yu, H. Dong, C. Liu, H. Wu, H. Che, G. Chen, Appl. Catal. B 238 (2018) 284–293.
[62] W. Yu, J. Chen, T. Shang, L. Chen, L. Gu, T. Peng, Appl. Catal. B 219 (2017) 693–704.
[63] J. Tang, R. Guo, W. Zhou, C. Huang, W. Pan, Appl. Catal. B 237 (2018) 802–810.
[64] S. Huang, Y. Xu, T. Zhou, M. Xie, Y. Ma, Q. Liu, L. Jing, H. Xu, H. Li, Appl. Catal. B 225 (2018) 40–50.
[65] H. Yu, R. Shi, Y. Zhao, T. Bian, Y. Zhao, C. Zhou, G.I.N. Waterhouse, L.Z. Wu, C.H. Tung, T. Zhang, Adv. Mater. (2017) 29.
[66] J. Zhao, J. Nan, Z. Zhao, N. Li, J. Liu, F. Cui, Appl. Catal. B 202 (2017) 509–517.
[67] K. Tsuji, O. Tomita, M. Higashi, R. Abe, ChemSusChem 9 (2016) 2201–2208.
[68] F. Wang, W. Li, S. Gu, H. Li, C. Ren, X. Liu, Eur. J. Inorg. Chem. 2018 (2018) 2564–2573.
[69] H. Li, W. Li, S. Gu, F. Wang, H. Zhou, Catal. Sci. Technol. 6 (2016) 3510–3519.
[70] F. Wang, W. Li, S. Gu, H. Li, X. Wu, X. Liu, Chem. Eur. J. 22 (2016) 12859–12867.
[71] Z. Jiang, W. Wan, H. Li, S. Yuan, H. Zhao, P.K. Wong, Adv. Mater. (2018) 30.
[72] L. Tian, X. Yang, Q. Liu, F. Qu, H. Tang, Appl. Surf. Sci. 455 (2018) 403–409.
[73] Q. Liu, J. Shen, X. Yang, T. Zhang, H. Tang, Appl. Catal. B 232 (2018) 562–573.
[74] P.M. Wood, Biochem. J. 253 (1988) 287–289.
[75] F. Dong, Z. Wang, Y. Li, W.K. Ho, S.C. Lee, Environ. Sci. Technol. 48 (2014) 10345–10353.